

WILEY-VCH



European Chemical  
Societies Publishing

# Take Advantage and Publish Open Access



By publishing your paper open access, you'll be making it immediately freely available to anyone everywhere in the world.

That's maximum access and visibility worldwide with the same rigor of peer review you would expect from any high-quality journal.

**Submit your paper today.**



[www.chemistry-europe.org](http://www.chemistry-europe.org)

# Controlling the Production of Acid Catalyzed Products of Furfural Hydrogenation by Pd/TiO<sub>2</sub>

George F. Tierney,<sup>[a, b]</sup> Shahram Alijani,<sup>[c]</sup> Monik Panchal,<sup>[b, d]</sup> Donato Decarolis,<sup>[b, e]</sup> Martha Briceno de Gutierrez,<sup>[f]</sup> Khaled M. H. Mohammed,<sup>[a]</sup> June Callison,<sup>[b, e]</sup> Emma K. Gibson,<sup>[g]</sup> Paul B. J. Thompson,<sup>[h, i]</sup> Paul Collier,<sup>[f]</sup> Nikolaos Dimitratos,<sup>[j]</sup> E. Crina Corbos,<sup>[f]</sup> Frederic Pelletier,<sup>[f]</sup> Alberto Villa,<sup>\*[c]</sup> and Peter P. Wells<sup>\*[a, b, k]</sup>

We demonstrate a modified sol-immobilization procedure using (MeOH)<sub>x</sub>/(H<sub>2</sub>O)<sub>1-x</sub> solvent mixtures to prepare Pd/TiO<sub>2</sub> catalysts that are able to reduce the formation of acid catalyzed products, e.g. ethers, for the hydrogenation of furfural. Transmission electron microscopy found a significant increase in polyvinyl alcohol (PVA) deposition at the metal-support interface and temperature programmed reduction found a reduced uptake of hydrogen, compared to an established Pd/TiO<sub>2</sub>

preparation. We propose that the additional PVA hinders hydrogen spillover onto the TiO<sub>2</sub> support and limits the formation of Brønsted acid sites, required to produce ethers. Elsewhere, the new preparation route was able to successfully anchor colloidal Pd to the TiO<sub>2</sub> surface, without the need for acidification. This work demonstrates the potential for minimizing process steps as well as optimizing catalyst selectivity – both important objectives for sustainable chemistry.

## Introduction

The behaviour of supported nanoparticle (NP) catalysts is both exceedingly dynamic, evolving with changes to reaction conditions, and sensitive, e.g. highly dependent on subtle alterations of preparation. The understanding of how these adaptations can be effectively exploited has become a significant aspect of catalytic science. On this topic, supported palladium NPs have proven to be a very effective class of catalysts and there are many ways in which they can be prepared.<sup>[1–6]</sup> Of these, sol-immobilization has proven a very attractive process

that is able to produce tailored NPs through systematic investigations of the synthesis parameters. In general terms, the synthetic process can be divided into four stages: (i) chemical reduction of the precursor metal salt (e.g. Na<sub>2</sub>[PdCl<sub>4</sub>]), (ii) capping of the formed colloids using a stabilizer (e.g. poly-vinyl alcohol (PVA)), (iii) immobilization of the colloidal, and (iv) filtration, washing and drying of the catalyst slurry. The systematic studies to date have focussed on the choice of reducing agent,<sup>[2,7]</sup> synthesis temperature,<sup>[8,9]</sup> precursor concentration,<sup>[10,11]</sup> and the nature of the stabilizing agent employed (electrostatic, steric stabiliser).<sup>[12–15]</sup>

[a] G. F. Tierney, Dr. K. M. H. Mohammed, Dr. P. P. Wells  
School of Chemistry  
University of Southampton  
Southampton, SO17 1BJ (UK)  
E-mail: ppwells@soton.ac.uk

[b] G. F. Tierney, M. Panchal, Dr. D. Decarolis, Dr. J. Callison, Dr. P. P. Wells  
UK Catalysis Hub  
Research Complex at Harwell, Rutherford Appleton Laboratory  
Harwell, Didcot, OX11 0FA (UK)

[c] Dr. S. Alijani, Prof. A. Villa  
Dipartimento di Chimica,  
Università degli Studi di Milano  
20133, Milano (Italy)  
E-mail: alberto.villa@unimi.it

[d] M. Panchal  
Department of Chemistry  
University College London  
London, WC1H 0AJ (UK)

[e] Dr. D. Decarolis, Dr. J. Callison  
Cardiff Catalysis Institute  
School of Chemistry  
Cardiff University  
Cardiff, CF10 3AT (UK)

[f] Dr. M. B. de Gutierrez, Dr. P. Collier, Dr. E. C. Corbos, Dr. F. Pelletier  
Johnson Matthey Technology Centre  
Sonning Common, Reading, RG4 9NH (UK)

[g] Dr. E. K. Gibson  
School of Chemistry  
University of Glasgow  
Glasgow G12 8QQ (UK)


[h] P. B. J. Thompson  
BM28/XMaS UK CRG  
ESRF  
38043 Grenoble (France)

[i] P. B. J. Thompson  
Oliver Lodge Laboratory  
Department of Physics  
University of Liverpool  
Liverpool L69 7ZE (UK)

[j] Prof. N. Dimitratos  
Dipartimento di Chimica Industriale  
"Toso Montanari" Alma Mater Studiorum Università di Bologna  
40136 Bologna (Italy)

[k] Dr. P. P. Wells  
Diamond Light Source  
Harwell Science and Innovation Campus  
Chilton, Didcot OX11 0DE (UK)

 Supporting information for this article is available on the WWW under <https://doi.org/10.1002/cctc.202101036>

 © 2021 The Authors. ChemCatChem published by Wiley-VCH GmbH. This is an open access article under the terms of the Creative Commons Attribution License, which permits use, distribution and reproduction in any medium, provided the original work is properly cited.

Amongst these elegant studies, there is a general consensus that optimising NP size (<3 nm) would correlate with high activity. Without the presence of a stabilizer there is a direct correlation between NP size and active catalyst surface area. However, the use of a stabilizer complicates this relationship as it alters the availability of substrate binding sites on NP surfaces.<sup>[14,15]</sup> In this regard, we recently reported on the use of mixed solvent mixtures (e.g. ethanol/H<sub>2</sub>O) in the preparation of Pd/TiO<sub>2</sub>. The outcome of this study was that the choice of solvent impacted the stabilizer-metal interaction, allowing control of both the NP size and what sites were available.

The hydrogenation of furfural, towards furfuryl alcohol (FA) or tetrahydrofurfuryl alcohol (THFA), used for manufacturing resins<sup>[16]</sup> and as an agricultural solvent,<sup>[17]</sup> respectively, is a crucial process in upgrading waste biomass within the sustainable chemicals industry.<sup>[18–23]</sup> The upgrading of such highly functionalised molecules requires a high degree of specificity to limit the generation of by-products. In our previous study, the nature of furfural binding sites and the selectivity to either hydrogenation product could be tuned by the choice of solvent conditions used in catalyst preparation. However, one aspect this adapted preparation could not address was the generation of ether by-products.

In this study we report how systematic changes to the solvent of synthesis, specifically the use of methanol, affords the formation of NPs with tailored characteristic, whilst simultaneously allowing for the removal of process steps. Using methanol, and methanol-water mixtures, was able to achieve a high degree of immobilisation without the need of support acidification (Figure S1). Moreover, the Pd/TiO<sub>2</sub> catalysts prepared using methanol as part of the solvent mixture were more directed towards the hydrogenation products of furfural, suppressing the ether by-products.

## Results and Discussion

**Characterisation of prepared catalysts.** The nomenclature (Table 1) of the presented catalysts describes the choice of synthesis solvent (W = water, Me = methanol), the inclusion of a stabilizing agent (P = PVA used), and if support acidification was performed (A = acidification performed). Solutions of Na<sub>2</sub>[PdCl<sub>4</sub>] (0.128 mM) were prepared in water, methanol, and water-methanol (MeOH)<sub>x</sub>/(H<sub>2</sub>O)<sub>1-x</sub> solvent mixtures (x = 0, 0.5, or 1) and characterized by UV-Vis spectroscopy (Figure S2a–c). The

[PdCl<sub>4</sub>]<sup>2-</sup> anion exhibits ligand to metal charge transfer (LMCT) absorbance bands at 210, 238, and 329 nm, alongside a *d-d* transition at 410 nm.<sup>[24–26]</sup> These bands were observed for the precursor solutions of PdWPA, PdWP, and PdW. However, when using methanol in the precursor solution (i.e. for Pd50MeP, PdMeP, Pd50Me and PdMe) shifts in the distinctive LMCT and *d-d* transitions were observed. This confirms a change to the Pd metal precursor complex when it is solvated in either the MeOH/H<sub>2</sub>O mixture or in pure MeOH. This can be rationalised by an exchange of Cl by MeOH, which has previously been shown to shift the observed transitions to lower wavelengths, as found in this work.<sup>[27]</sup> Once reduced, the appearance of a broad absorbance band across the spectra was shown for all solutions, confirming the formation of Pd colloids (Figure S2d).<sup>[18,28]</sup> The colloidal solutions were subsequently anchored onto P25 TiO<sub>2</sub> without acidification of the support, except for PdWPA, where the solution was acidified to pH 1–2 upon immobilization (Table 1).

The Pd wt% loading of each catalyst was determined using microwave plasma – atomic emission spectroscopy (MP-AES) (Table S1). Preparation of the Pd/TiO<sub>2</sub> following a standard route, including acidification and a water solvent system (PdWPA), achieved a Pd loading of 0.83 wt%, as is commonly found.<sup>[18]</sup> Removal of the acidification step results in a reduced Pd loading for PdWP (0.25 wt%) and PdW (0.3 wt%) (Table 1). The decrease in loading is consistent with previous work that found acidification is required for adhesion of the colloid to the TiO<sub>2</sub> surface.<sup>[29]</sup> Conversely, when the acidification step is removed and MeOH is present in solvent, similar (PdMeP = 0.86%) and higher (PdMe = 0.96%) levels of immobilization were observed. We subsequently prepared catalysts with incremental loadings of Pd, e.g. 2.5, 5, 7.5 and 10 wt% Pd, and found no significant detriment to immobilization at increased Pd content, e.g. the 10 wt% analogue had a Pd loading of 8.9 wt% (Figure S3). In addition, the adaptability of our MeOH based synthesis was measured in the immobilization of Pd NPs onto different supports; SiC, SiO<sub>2</sub>, ZnO, MgO, Fe<sub>2</sub>O<sub>3</sub> and CeO<sub>2</sub> (Table S2). Our updated method provides comparable, if not better loadings than the WPA counterparts. However, we did observe low loadings (0.03 wt% Pd) when immobilizing the MeOH prepared NPs onto both SiO<sub>2</sub> and Fe<sub>2</sub>O<sub>3</sub>.

Sulfur is a known poison for many reactions involving Pd NPs and the removal of acidification has the potential to change the residual S environments present.<sup>[30–32]</sup> To assess this we utilised S K-edge X-ray absorption near edge structure

**Table 1.** Temperature and synthetic conditions applied in the preparation for each Pd/TiO<sub>2</sub> catalyst. All catalysts were prepared at a constant temperature of 1 °C. Pd loading was measured using MP-AES, average Pd nanoparticle size was assessed using TEM imaging counting 200–300 particles per sample.

Catalyst	MeOH [vol.%]	PVA stabilization	Acidification of catalyst slurry	MP-AES [Pd] [wt.%]	TEM NP size [nm]
PdWPA	0			0.83	2.6 ± 1.4
PdWP	0		×	0.25	1.7 ± 0.7
Pd50MeP	50		×	0.91	1.7 ± 0.7
PdMeP	100		×	0.86	1.8 ± 0.8
PdW	0		×	0.30	3.1 ± 1.5
Pd50Me	50	×	×	0.91	3.6 ± 1.6
PdMe	100	×	×	0.96	3.3 ± 2.3

(XANES) analysis (Figure 1, Figure S4). The presence of sulfur was observed on all catalysts, however, the intensity of the S fluorescence intensity was significantly higher for PdWPA – the only catalyst that used an acidification step with  $\text{H}_2\text{SO}_4$ . The S K-edge XANES spectrum of PdWPA shows a distinct white line peak at 2482 eV, and is identified as sulfur in the  $\text{S}^{6+}$  oxidation state (e.g.  $\text{SO}_4^{2-}$ ).<sup>[33,34]</sup> A low intensity peak is also observed for all samples at  $\sim 2472$  eV. Features at this position have been ascribed to  $\text{S}^0$ , sulfide formation, or Pd–S interactions. However, the limited S K-edge XANES literature for these systems and the negligible energy shifts of this feature makes accurate assignment difficult.<sup>[33,35–38]</sup> From our data we have demonstrated that

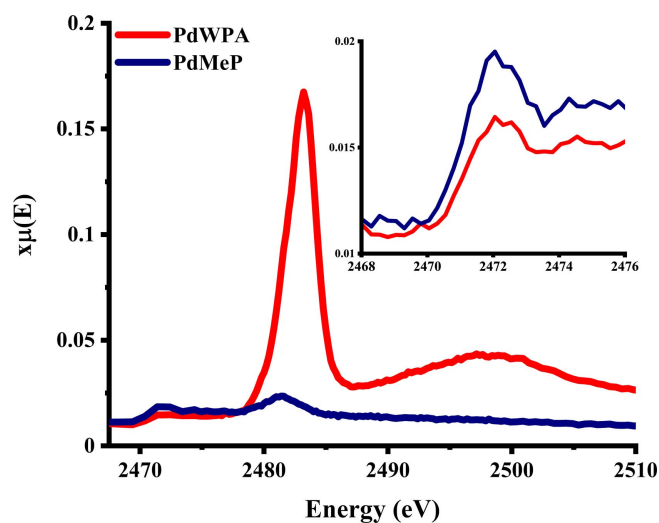


Figure 1. S K-edge XANES region for samples PdWPA and PdMeP. Insert is the expanded XANES profile for the pre-edge region.

our adapted synthetic protocol is able to significantly reduce the residual S present within supported Pd NP catalysts.

All powdered catalysts were characterised using transmission electron microscopy (TEM), with their average NP sizes and particle size distributions/dispersions evaluated using ImageJ software (Figures S5, S6).<sup>[39]</sup> An initial comparison of catalysts PdWPA and PdWP, shows that an acidified immobilization step increases the average NP size (PdWP = 1.7 nm, PdWPA = 2.6 nm), agreeing with our previous work in this area.<sup>[10]</sup> However, it is important to note there is a stark decrease in Pd loading for PdWP (0.25 wt%).

The greater NP size observed for PdWPA has previously been ascribed to the interaction of the stabilising agent with the acid during the immobilization phase; as the acid is added to the catalyst slurry, it strips away the PVA from the NP surface, leading to the aggregation of the NPs.<sup>[40]</sup> However, the acidification is required to ensure higher Pd loadings when using water as a solvent. The samples prepared using MeOH (PdMeP and Pd50MeP) achieved good immobilization without acidification and led to smaller average Pd NP sizes compared to PdWPA (Pd50MeP = 1.7 nm, PdMeP = 1.8 nm). We also found that the absence of PVA (i.e. PdMe) yields Pd NPs with greater instances of particle agglomeration on the support surface; agreeing with prior studies on the importance of the stabilising agent.<sup>[12–15]</sup> These findings were further supported by scanning transmission electron microscopy (STEM) using a high angle annular dark field detector (HAADF), coupled with energy dispersive X-ray (EDX) analysis (Figure 2).

The characteristic frequency of CO stretching vibrations, using probe molecule adsorption FTIR, is effective for understanding the nature of available surface.<sup>[18,41–44]</sup> The characteristic CO adsorption bands for PdMe, PdMeP, and PdWPA (Figure 2) are: (i) a peak at  $\sim 1875\text{ cm}^{-1}$  that describes the

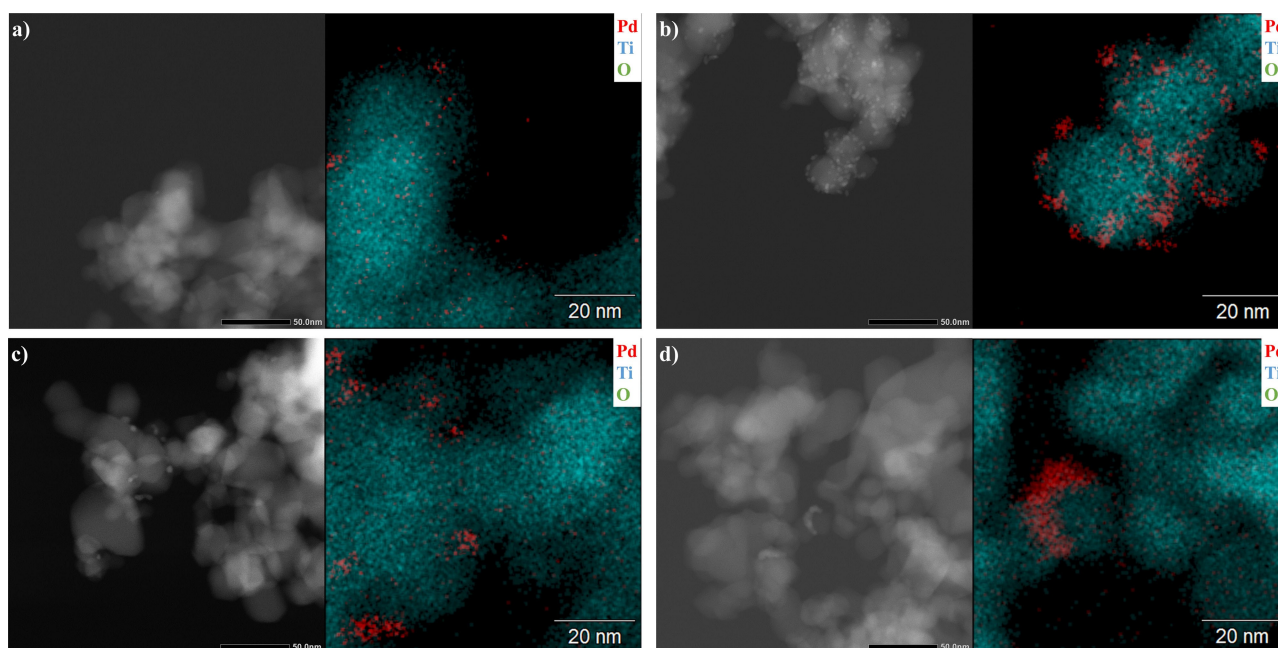
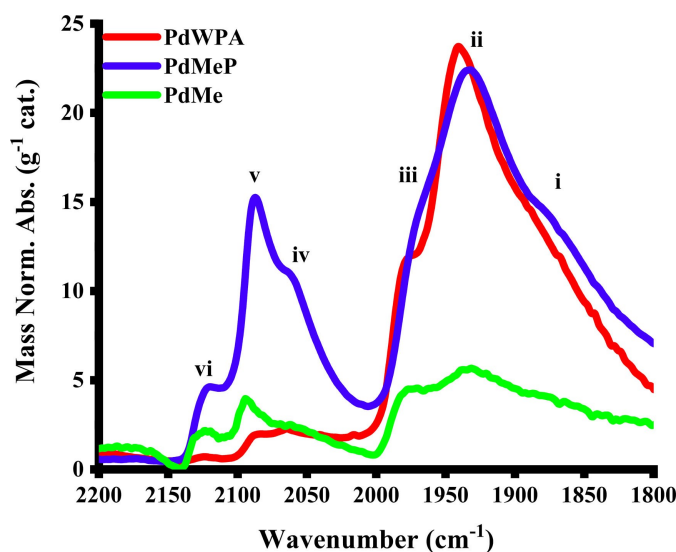
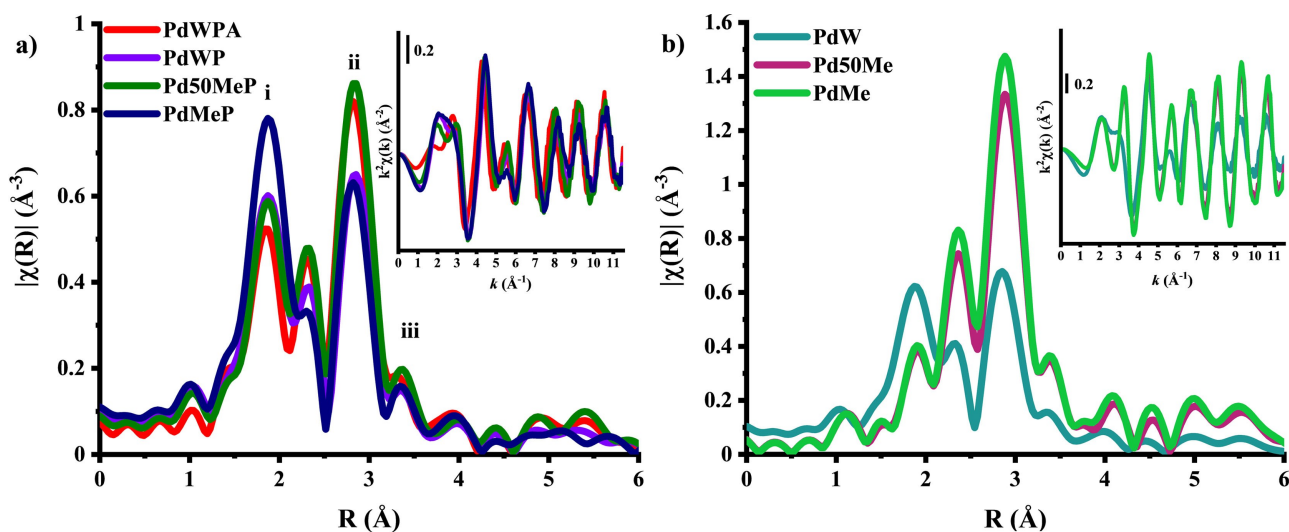


Figure 2. STEM HAADF images and corresponding EDX maps of (a) PdWP, (b) PdMeP, (c) PdW, and (d) PdMe.

adsorption on 3-fold surface sites;<sup>[45,46]</sup> (ii) and (iii) represent adsorption band at  $\sim 1975$  and  $1945\text{ cm}^{-1}$  from bridge-bonding of CO, which shift to higher wavenumber as a result of dipole-dipole coupling of adsorbed CO;<sup>[47–49]</sup> (iv) and (v) at  $\sim 2063$  and  $2086\text{ cm}^{-1}$  are assigned to CO linearly adsorbed on edge and corner sites of Pd NPs, respectively,<sup>[50]</sup> finally (vi) a peak at  $\sim 2120\text{ cm}^{-1}$  from the adsorption of CO Pd<sup>+</sup>.<sup>[45,46]</sup> In this study, the relative intensity of the CO adsorption bands through transmission FTIR studies are indicative of the total number of adsorption sites per unit mass. Assessing the relative intensities of the CO adsorption bands in Figure 3, the PdMe catalyst has a much lower CO coverage per gram of catalyst. This is a consequence of the dense agglomeration observed in the TEM. However, for PdMe there is a high relative fraction of bands



**Figure 3.** CO probe molecule FTIR analysis performed on catalysts PdWPA, PdMeP and PdMe. Bands i–vi are described as bridged (i–iii) and linear (iv–vi) CO adsorption to the Pd NPs.



**Figure 4.** Pd K-edge magnitude FT and chi XAFS data for (a) PdWPA, PdWP, Pd50MeP, and PdMeP, and (b) PdW, Pd50Me, and PdMe.

with linear adsorbed CO on well resolved corner sites. On the inclusion of PVA, the stabilising effect limits the coalescence of Pd and the total number of surface adsorption sites is greater than for PdMe.<sup>[12,14,18]</sup> Elsewhere, we observe a greater linear: bridged CO ratio for PdMeP compared to PdWPA. This provides a greater number of sites for binding the aldehyde functionality of furfural, and should promote the hydrogenation pathway towards furfuryl alcohol, as has been reported previously.

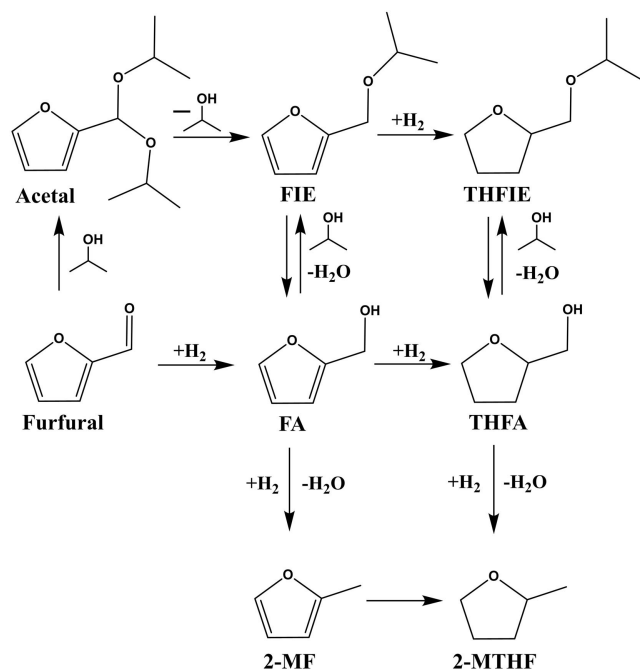
X-ray absorption fine structure (XAFS) was also used to assess changes to Pd oxidation state (X-ray absorption near edge structure - XANES) and the local structural environment with respect to Pd (extended X-ray absorption near edge structure - EXAFS) (Figure 4).<sup>[51]</sup> The per atom average provided by XAFS allowed the zero-valent (Pd<sup>0</sup>) and oxidised (Pd<sup>2+</sup>) components of the catalysts to be calculated through linear combination analysis (LCA) of the XANES region (Figure S7, Table S3). The LCA identifies two competing factors that influence the amount of Pd<sup>2+</sup> - particle size and the presence of PVA. Pd surfaces are known to form passivating oxide layers on exposure to air with increased temperature required to form a bulk oxide structure. Ultimately, the Pd<sup>2+</sup> fraction corresponds to the amount of available Pd surface and therefore particle size.

However, in this series there are examples where this particle size trend is not uniform, e.g. PdW (Pd<sup>2+</sup> fraction = 32.4%) has a comparable oxidic fraction to PdWP (31.9%), despite having a larger particle size (3.1 vs 1.7 nm). Elsewhere, the PdMeP catalyst has a larger oxidic fraction (~41%) than other systems of other systems of comparable particle size. This information is in agreement with the CO adsorption FTIR data, which demonstrates that amount of accessible surface is influenced both by particle size and surface site accessibility; the latter of these points is controlled by the metal-stabilizer interaction, which is influenced by the choice of solvent.

Analysis and fitting of the higher energy EXAFS region agreed with the characterization discussed previously (Fig-

ure S8, Table S3 and S4). The formation of small Pd NPs were identified through: (i) the presence of a Pd–O scattering path at 1.7 Å, indicative of the passivated oxide layer;<sup>[52]</sup> (ii) a decrease in the magnitude of the 1st shell Pd–Pd scattering path (~2.8 Å), with respect to a Pd foil; and (iii) the formation of large crystalline PdO phases is discounted by the absence of a Pd–O scattering path at 3 Å.<sup>[52]</sup>

**Catalytic activity testing.** All catalysts were evaluated for the hydrogenation of furfural at 50 °C (Scheme 1, Figure 5). The reaction conditions were optimised based on previous work to ensure operation under kinetic regime.<sup>[18]</sup> The XANES, EXAFS, and TEM data have all confirmed that PdMeP contains smaller NPs than PdWPA. However, the initial catalytic activity confirms that PdWPA has a significant increase in initial TOF (288 mol (mol Pd<sup>-1</sup>) hr<sup>-1</sup>, vs. 195 mol (mol Pd<sup>-1</sup>) hr<sup>-1</sup>) (Figure 5a, Table S5). Considering that PdMeP is known to contain smaller particles, why is it less active? Although the absolute conversion suggests a stark change in performance, analysis of the product distribution goes some way to rationalising this. The initial yield (i.e. at the same time point as the TOF calculation) of products derived from the major hydrogenation processes (i.e. FA, THFA) for PdWPA and PdMeP are 8.3% and 6.7%, respectively. The selectivity at isoconversion and product yields for all catalysts can be found in the supplementary datasets for this work, Figures S9–S12, Tables S6–7. There is still an observable difference between these two values, but it is not the increase the TOF would imply. The other major product produced from PdWPA is the acetal, (2-(diisopropoxymethyl) furan, that arises



**Scheme 1.** Possible reaction pathways of furfural hydrogenation. Reaction products shown are: furfuryl alcohol (FA), tetrahydrofurfuryl alcohol (THFA), furfuryl isopropyl ether (FIE), tetrahydrofurfuryl isopropyl ether (THFIE), 2-methylfuran (2-MF), 2-methyltetrahydrofuran (2-MTHF) and 2-(diisopropoxymethyl) furan (Acetal). Products FIE, THFIE, 2-MF, 2-MTHF and acetal are denoted as ‘ether’ in presentation of hydrogenation data.

from the direct reaction of furfural with 2-propanol (isopropyl alcohol (IPA)), that forms selectively over TiO<sub>2</sub> surfaces.<sup>[53,54]</sup>

In this work, we found that furfural hydrogenation performed over the bare TiO<sub>2</sub> support displayed 98.4% selectivity to the acetal (2-(diisopropoxymethyl) furan, Table S7, Figure S13).

The increase in activity can, to a significant extent, be rationalised by the presence of additional Brønsted acid sites to produce acetals. The same influence catalysis is also seen when we consider the selectivity distribution after 5 hours of reaction time (Figure 5). The relative yield of all ether products is reduced for catalysts where both methanol in the solvent and PVA have been used, e.g. PdMeP has a total ether yield of 5.8%, whereas PdWPA has a total ether yield of 22.8%. Furthermore, the selectivity to hydrogenation products FA and THFA for PdMeP and PdWPA, were 47.9 and 50.0%, respectively. This is noteworthy as PdWPA has ~22% increase in furfural conversion at 5 hours of reaction time. Where, the Pd/TiO<sub>2</sub> catalysts have been prepared using methanol as a solvent, but in the absence of PVA (e.g. PdMe and Pd50Me), we do not find the same preference for hydrogenation products over the production of ethers. For example, PdMe produces a greater yield of ether products than PdMeP (8.5% vs. 5.8%), although the overall conversion is significantly lower. To understand these differences in activity/selectivity we performed further HRTEM investigations of the fresh PdMeP (Figure 6). These studies identified a thick amorphous layering of PVA surrounding the NPs produced using MeOH (e.g. PdMeP) and at the interface between the NPs and the support. We propose that the poor solubility of PVA in methanol is responsible for this increase clustering of PVA on the catalyst surface/support interface. This clustering of PVA then reduces access to interfacial sites.

The properties of the polymer stabilizer used during sol-immobilization synthesis are also worth consideration when designing and preparing colloidal nanoparticles via this method. In the main, a long chain polymer, such as PVA, will associate with the NP through steric interactions, non-bonding interactions, or a weak interaction between –OH functionality.<sup>[55,56]</sup> In colloidal solutions, it is the presence of the capping agent around a NP, and the electrostatic, or in the case of PVA's, steric repulsion between like capped NPs that prevents the colloid from collapsing.<sup>[57]</sup> Moreover, Chowdhury *et al.* described a change in the available surface sites on PVA capped Pd NPs by introducing EtOH into the synthesis solvent. Here, the interactions of H<sub>2</sub>O and PVA in the solution decreased, with EtOH–H<sub>2</sub>O becoming the norm. With this, the –OH functionalities of PVA bound with greater strength to the Pd surface, increasing the encapsulation of the NP, and reducing the access to surface active sites.<sup>[58]</sup> The extent to which the catalyst surface is blocked by the stabiliser and its sterics has also been discussed by Medlin *et al.*, wherein the sterics of the capping agent had influence on how furfural could bind to edge and terrace sites, resulting in hydrogenation or decarbonylation reactions occurring, respectively.<sup>[15]</sup> Moreover, the extent of the polymer chain length has also been reported to influence NP size and activity. One such study was published by Dimitratos *et*

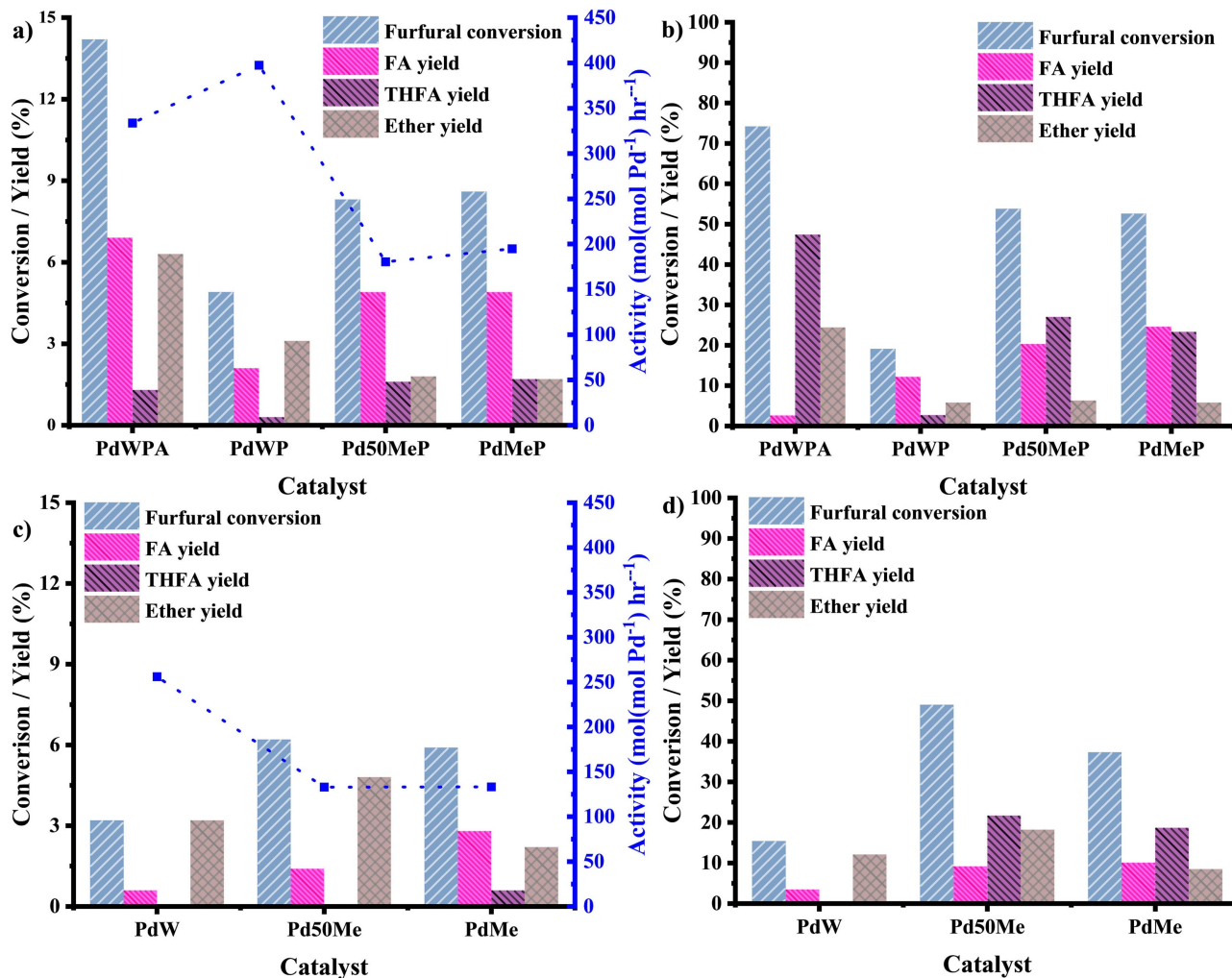


**Figure 5.** Catalytic performance plots for hydrogenation of furfural using Pd/TiO<sub>2</sub> catalysts synthesised following variations to protocol stated previously. Conversion and selectivity were calculated after: a & c) 15 minutes and b & d) 5 hours. Reaction conditions: furfural 0.3 M, furfural./metal ratio 500 mol/mol, 5 bar H<sub>2</sub>, solvent: 2-propanol. Ether yield is presented as a grouping of the undesired by-products of FIE, THFIE, 2-MF, 2-MTHF and acetal.

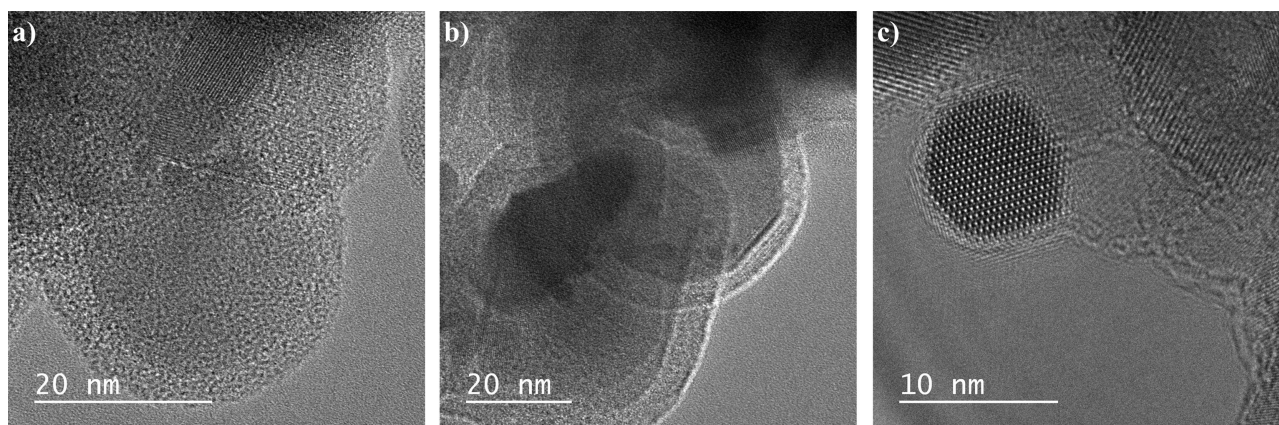


**Figure 6.** HRTEM images of fresh PdMeP. Layering of the organic PVA can be seen surrounding both the titania support (a & b) as well as the Pd NPs (c)

al, where they reported that encapsulation of colloidal Au NPs with longer polymer chains ( $M_w \geq 23,300 \text{ g mol}^{-1}$ ). Capping of

the Au colloid using PVA with high  $M_w$  proved to be preferential for ensuring a stable colloid, however, the final

supported NP catalyst displayed decreased catalytic activity.<sup>[59]</sup> This was rationalized by increased steric and electronic effects of the polymer chains inhibiting access to the catalyst surface, and has been corroborated by similar studies of PVP-capped Au colloids.<sup>[60]</sup>

The conversion to acetals requires Brønsted acid sites on the TiO<sub>2</sub> surface.<sup>[61,62]</sup> We recently published an article on Pd/NiO catalysts and were able to demonstrate a dual-site hydrogenation mechanism, where spillover of hydrogen onto the NiO support was a significant part of the reaction pathway.<sup>[63]</sup> For TiO<sub>2</sub>, hydrogen spillover creates surface hydroxyls that are able to act as Brønsted acid sites required for ether formation.<sup>[64,65]</sup> It has already been established that the generation of surface hydroxyls on TiO<sub>2</sub> can be enhanced through hydrogen spillover, and that this has been linked to the production of ethers.<sup>[66,67]</sup>

Furthermore, the role of dual-site catalytic mechanisms of Pd/TiO<sub>2</sub>, facilitated by hydrogen spillover from Pd to TiO<sub>2</sub> has been found previously.<sup>[68]</sup> Surfaces of TiO<sub>2</sub> also contain catalytically active Lewis acid sites, however, recent studies have shown that without the presence of Brønsted acid functionalities, furfural cannot be readily converted to furanic ethers.<sup>[69]</sup> Another possibility for the generation of Brønsted acid sites could be accounted for by the presence of residual halide; recently, it has been proposed that Pd–X interactions allow for heterolytic H–H cleavage which gives rise to Brønsted acidity.<sup>[70]</sup>

To assess how the preparation method influences the residual Cl speciation we performed a Cl K edge XANES study. We observed a marked difference in the Cl environment before and after reduction of the Pd precursor salt (Figure 7a & b and S14). In the initial spectrum of the precursor complex a distinct pre-edge peak positioned at 2821.7 eV represents the dipole-allowed Cl 1s→3p transition to the doubly degenerate LUMO of the precursor complex, where the LUMO has predominantly Cl 3p and Pd 4d<sub>x<sup>2</sup>-y<sup>2</sup></sub> character (Figure 7a).<sup>[71–73]</sup> Ultimately, a feature at this position is indicative of Pd–Cl interactions. After

reduction and support immobilization, a shoulder at ~2821.7 eV can be seen for the prepared catalysts. The presence of unreduced Na<sub>2</sub>PdCl<sub>4</sub> can be discounted as full reduction of the salt is shown in the UV-Vis spectra (Figure S2d). We rationalise that this Cl signal arises from adsorbed chloride on the Pd surface as others have also reported.<sup>[74,75]</sup> Between samples PdWPA and PdMeP, this feature has comparable intensity, suggesting a similar amount of surface Cl, however we see no selection to the acid catalysed product for PdMeP. If adsorbed halide species were to be the governing factor for promoting Brønsted acid sites, we would expect both catalysts to have comparable selectivity. In our work, we found no evidence that the selectivity profile was controlled as a result of Pd–X interactions. To understand the influence the colloidal solvent has on the accessibility of TiO<sub>2</sub> Brønsted acid sites, we utilised hydrogen temperature programmed reduction (H<sub>2</sub>-TPR) to measure the uptake of H<sub>2</sub> for the PdWPA and PdMeP catalysts (Figure 8). The H<sub>2</sub>-TPR data for both catalyst exhibits three features below 350 °C: (I) a negative peak at ~50 °C, which is assigned to the decomposition of Pd hydride,<sup>[76–80]</sup> (II) an additional negative peak between 100–150 °C that is indicative of dehydration,<sup>[81]</sup> and (III) a positive feature between 200–350 °C that has been reported as the reduction of Ti<sup>4+</sup> to Ti<sup>3+</sup> in the vicinity of Pd, *i.e.*, hydrogen spillover from Pd to the support.<sup>[82,83]</sup>

Comparing the TPR traces for PdWPA and PdMeP, it is clear that the amount of hydrogen through spillover is far greater for PdWPA (1.64 μL/g Pd) than PdMeP (0.10 μL/g Pd). Typically, in the absence of hydrogen spillover, reduction of Ti<sup>4+</sup> to Ti<sup>3+</sup> is found to occur at temperatures > 600 °C.<sup>[82]</sup> This observation is consistent with our hypothesis of a dual-site mechanism for our acid catalyzed products, which are produced most significantly for the PdWPA system. We performed both NH<sub>3</sub>-TPD and NH<sub>3</sub> adsorption using DRIFTS couple with MS (Figures S15–16). However, as a consequence of the carbonyl bands of PVA,

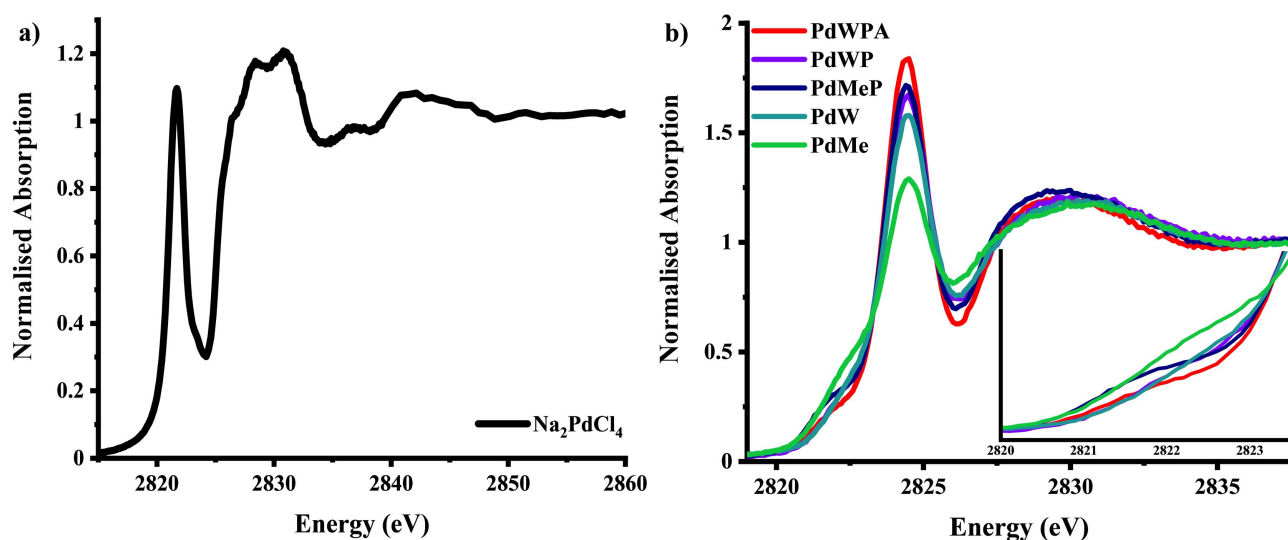


**Figure 7.** Normalised Cl K-edge XANES data acquired for the Pd precursor salt (a) and the prepared Pd/TiO<sub>2</sub> catalysts (b), the insert graph of figure b shows the shoulder peak at 2821.7 eV.



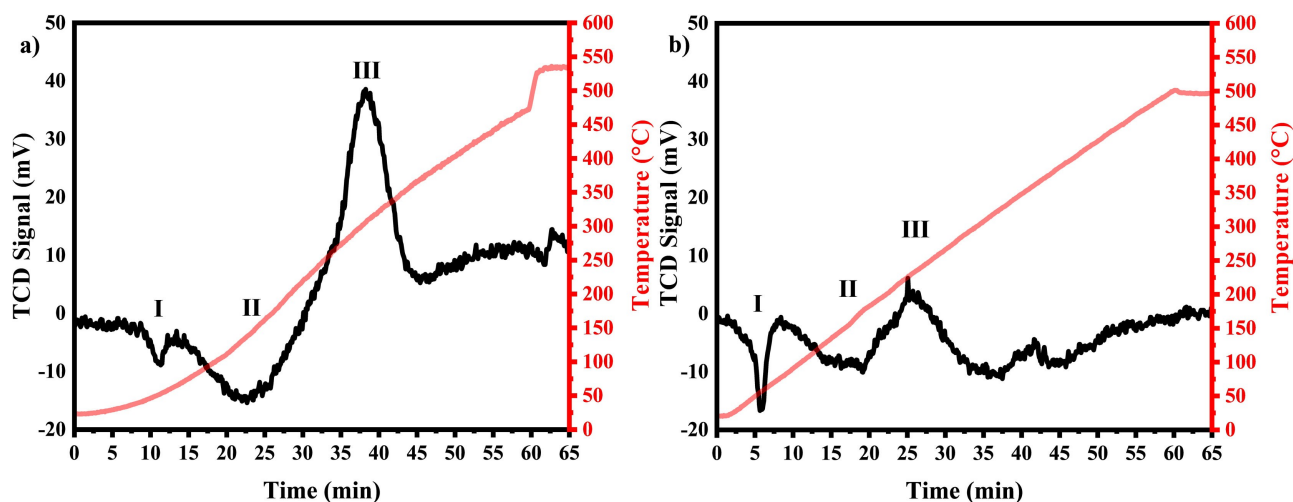


Figure 8. H<sub>2</sub>-TPR profiles of fresh catalysts: a) PdWPA, and b) PdMeP.

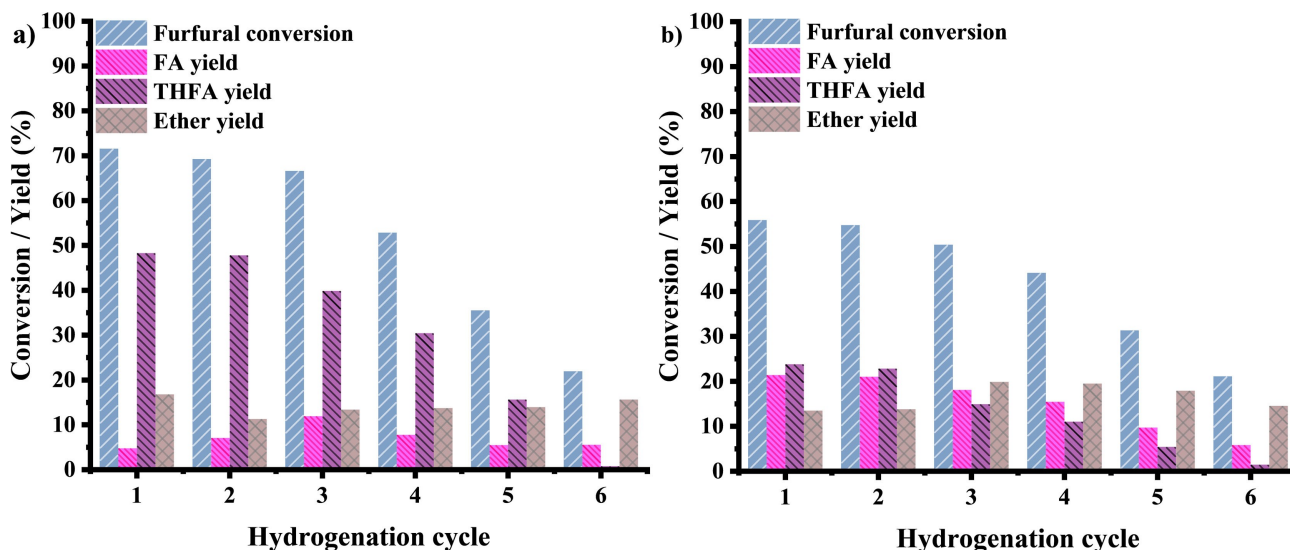


Figure 9. Catalytic performance plots for the hydrogenation of furfural over prepared Pd/TiO<sub>2</sub> catalysts. All catalysts were tested in 6 successive hydrogenation cycles. Catalysts were recovered from the previous test, dried and reused. Substrate conversion and product selectivities were calculated at 3 hours reaction time prepared catalysts: a) PdWPA and b) PdMeP. Reaction conditions: 50 °C, furfural 0.3 M; furfural:metal ratio 500 mol:mol, 5 bar H<sub>2</sub>, solvent: IPA. Ether yield is presented as a grouping of the undesired by-products of FIE, THFIE, 2-MF, 2-MTHF and acetal.

which appear in the region of interest (1700–1300 cm<sup>-1</sup>), we were unable to easily identify the bands of NH<sub>3</sub> adsorption on Brønsted acid sites (~1460 and 1689 cm<sup>-1</sup>). Pyridine adsorption would also result in bands in this area of the spectrum and so we did not pursue this further.<sup>[84]</sup> On this matter, there may be limited value in assessing the extent of acid sites on the initial catalyst, as they are likely to be generated *in situ*, during catalysis.

Returning to the catalytic activity of our Pd/TiO<sub>2</sub> catalysts, we evaluated the stability of the synthesised catalysts by performing six successive hydrogenation cycles (Figure 9, Figure S17, and Tables S9–11). The catalysts prepared without PVA, i.e. PdMe, quickly deactivated with almost negligible performance by the 6<sup>th</sup> successive cycle. However, there are two key

observations: (i) they both exhibit comparable activity and selectivity profiles after 6 successive cycles and (ii) the production of THFA drops to a negligible amount during the recyclability tests (PdWPA=0.8% yield, PdMeP=1.5% yield). The consistent selectivity profile for both PdMeP and PdWPA, with both producing a majority of acid catalyzed product, is concurrent with the progressive removal of PVA (PdWPA=0.9% acetal yield, PdMeP=1.1% acetal yield). The disappearance of THFA in the product distribution can be explained based on one of our previous findings: after successive cycles, the Pd NPs become carbided which is, in part, responsible for a loss in overall catalytic activity.<sup>[18]</sup> The carbidization, causes an expansion of the Pd–Pd distance, which has previously been shown to affect the nature of adsorption sites, using CO as probe

molecule. Our previous study has shown the carbidization causes a shift to a greater fraction of linear adsorbed CO species, and this change has been established to direct the FA/THFA selectivity. To assess the structural changes of these used catalysts in more detail, they were studied using STEM-HAADF analysis and XAFS spectroscopy (Figures 10 & 11, respectively).

**Characterisation of recycled catalysts.** The STEM analysis (Figure 10) of the spent sample shows, that when PVA is not present, the samples quickly agglomerate and effective surface area of Pd rapidly diminishes; for PdMe, particles with a diameter >20 nm are observed. The average particle size increases for all samples, however, in some cases only a relatively small fraction of particles was found (as a consequence of the agglomeration), which limits the accuracy of the particle size analysis. XAFS was subsequently used to provide a more definitive analysis of the extent of NP growth.

XANES acquired for the spent catalysts show a reduction in the appearance of an oxidised Pd state, through a decrease to the intensity of the main edge transition, often referred to as the 'white line' (Figure 11a–c), which is indicative of particle growth, i.e. a larger particle has a smaller fraction of oxidized surface particles.

Elsewhere, growth in particle size is also established through an increase in the 1<sup>st</sup> shell Pd–Pd coordination number, e.g. the Pd–Pd coordination number increases from 6.7 to 11.2 for WPA, which is conclusive evidence of significant particle growth (Figure S18, Table S12). This loss in effective metal surface area, is one of the key factors in reducing overall catalyst activity after the six successive cycles. The ability of Pd to form carbide nanoparticle on exposure to hydrocarbon reactant feeds at elevated temperature has been reported since the 1980s,<sup>[85,86]</sup> where the authors were able to correct previous

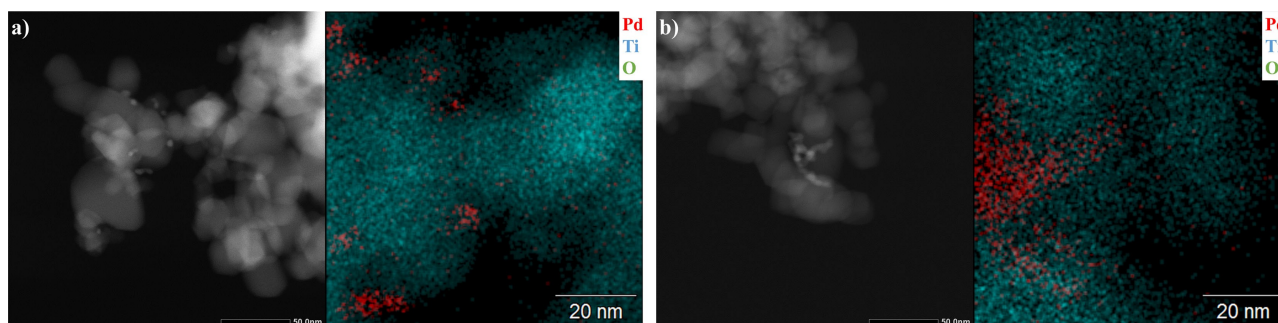


Figure 10. STEM-HAADF images of spent 1 wt % Pd/TiO<sub>2</sub> post furfural hydrogenation and their corresponding EDX maps: a) Used PdMeP, b) Used PdMe.

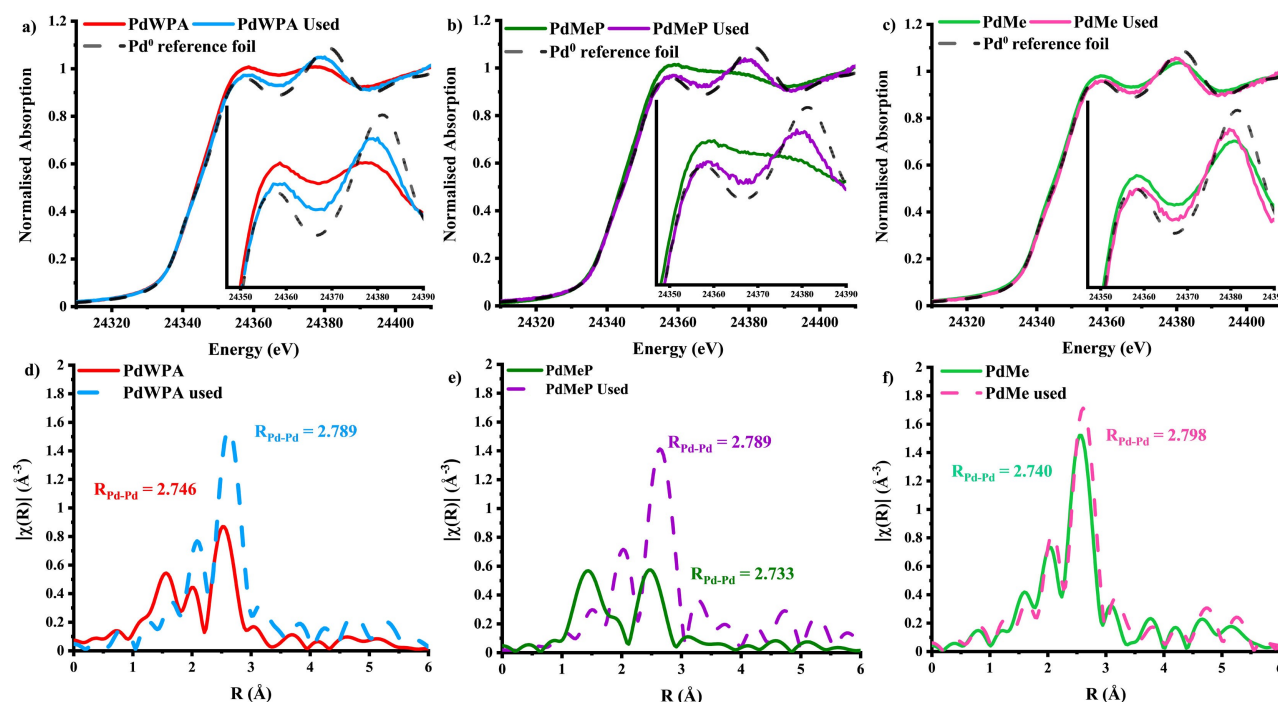


Figure 11. XAS spectra for the fresh and used catalysts, used data acquired after 6 successive hydrogenation cycles. Top row (a–c) XANES, bottom row (d–f) FT EXAFS data. PdWPA (a & d), PdMeP (b & e), PdMe (c & f). Expansions to the Pd lattice is observed for all FT EXAFS datasets.

literature in the 1970s that ascribed the lattice expansion on exposure to ethylene to the formation of Pd hydride.<sup>[87]</sup> Since then, there have been a variety of studies that have identified the formation Pd carbide using other hydrocarbon feeds, e.g. ethanol, CO, and pentyne.<sup>[86,88–91]</sup> The diffusion of carbon into the bulk lattice is limited for bulk Pd compared to their smaller nanoparticle counterparts and has led to the use of XANES and EXAFS to study the formation of Pd carbide. The structural information provided by XANES/EXAFS is not limited by the lack of long-range order and has provided more insight than diffraction based methods for the small nanoparticles typically used in heterogeneous catalysis.<sup>[92]</sup>

Such methods are now considered the mainstay of identification of Pd carbide.<sup>[93–96]</sup> The shift in the position of the second peak maximum is observed for both hydridic and carbidic forms of Pd; however, the broadening of the first peak is only observed for Pd carbide.<sup>[52,92]</sup> It is this specificity that allows us to assign the presence of Pd carbide for the spent catalysts in this study. Furthermore, the corresponding Fourier transforms of the chi-data further confirmed the formation of an interstitial structure type (Figure 11d–f). The significant shift in the Pd–Pd scattering magnitude toward a larger radial distance (R), is consistent with the formation of heteroatom inclusion into the Pd FCC lattice.<sup>[97]</sup> Such an expansion can also be found for Pd hydride, however, the XANES profile is not consistent with Pd hydride and the hydride phase is not stable in the absence of an overpressure of hydrogen.

## Conclusion

In this study, we report a modified sol-immobilization procedure for the preparation of supported Pd NPs using colloidal methods. The adapted colloidal method utilises MeOH within the solvent mixture during colloidal formation, yielding Pd/TiO<sub>2</sub> catalysts with an increased Pd loading compared to the conventional water based Pd/TiO<sub>2</sub> catalyst (PdWPA). Furthermore, particles with an average size of ~3 nm could be prepared in the absence of a capping agent. However, smaller Pd NPs (< 2 nm) were formed when using PVA as a stabiliser.

Elsewhere, the use of MeOH in the solvent mixture had a major impact on the hydrogenation of furfural; it suppressed the production of acid catalyzed by-products. The formation of acetals and ethers is rationalized by the spillover of hydrogen, creating surface hydroxyls, that occurs to a much greater extent for PdWPA compared to PdMeP, as found with H<sub>2</sub>-TPR measurements.<sup>[61,62]</sup> For the Pd nanoparticles prepared using MeOH as a solvent, a 'halo' of PVA at the metal-support interface was found, that we propose suppresses formation of Brønsted acid hydroxyls on the TiO<sub>2</sub> surface.

## Experimental Section

**Catalyst Preparation.** Supported Pd NPs were prepared following a standard sol-immobilisation method where the temperature of chemical reduction was kept at 1 °C. Pd colloids were prepared using [Na<sub>2</sub>[PdCl<sub>4</sub>]] solvated into solutions using deionised H<sub>2</sub>O

(18.2 MΩ cm) or MeOH (> 99% trace impurity, Sigma) to the desired Pd metal concentration (1.26 × 10<sup>-4</sup> M). For catalysts synthesised with the inclusion of a stabilising agent (PVA), an aqueous solution was prepared (PVA/Pd (w/w) = 0.65) and added. Solutions of NaBH<sub>4</sub> (0.1 M; NaBH<sub>4</sub>/Pd (mol/mol) = 5) were prepared fresh and added dropwise to each solution, over the course of a minute with stirring, to form dark brown-black sols. The solutions were left for 30 minutes as to fully reduce the Pd species, following this the sols were anchored onto TiO<sub>2</sub> (commercial P25) under vigorous stirring conditions, with the quantity of support material calculated to yield a final metal loadings of 1, 2.5, 5, 7.5 and 10 wt% Pd. Where required, the catalyst slurry was acidified to pH 1–2 using sulfuric acid. All catalyst slurries were left to stir for 1 hour to accomplish full immobilisation of the colloid to the metal oxide support. The catalyst slurries were filtered, washed thoroughly using deionised water, and dried overnight at room temperature (Figure S1).

**Ultra Violet-Visible Spectroscopy.** Reduction of the precursor Pd species was analysed using UV-Vis spectroscopy. 4 mL of the catalyst solution was analysed at a time, with samples taken at 0 mins, 15 mins and 30 mins. Full reduction of the Pd species was observed when a broad absorbance band appeared in the spectra (between 200–800 nm). Samples were characterised using a Shimadzu UV-1800 spectrophotometer in a quartz cuvette, using the synthesis solvent as a reference (i.e. MeOH was used for catalysts prepared using solely MeOH in the mother solvent).

**Transmission Electron Microscopy (TEM), Scanning TEM (STEM), High Angle Annular Dark Field and Bright Field STEM (HAADF & BF STEM), and High Resolution TEM (HRTEM).** Catalysts characterised for TEM, HAADF/BF STEM and HRTEM were prepared by crushing the powdered sample between two glass microscopy slides. Holey carbon mesh Cu TEM grids were passed through the powdered catalyst liberally and the excess was tapped off of the grids. TEM images were acquired using a JEOL JEM 2100 EM at the Research Complex at Harwell, Didcot, U.K. High angle annular dark-field (HAADF) atomic resolution and high resolution (HRTEM) imaging were performed using the probe-corrected JEOL ARM200CF Scanning TEM (STEM), operating at 200 kV, on Johnson Matthey's electron microscope at the I14 (ePSIC) beamline, Diamond Light Source (DLS), Didcot, U.K.

**Microwave Plasma – Atomic Emission Spectroscopy (MP-AES).** Pd metal wt% loadings were calculated using MP-AES, with the fresh Pd/TiO<sub>2</sub> catalysts (3 × 0.1 g) added to a solution of aqua regia (3:1 HCl: HNO<sub>3</sub>, Sigma, trace metal purities). These solutions were then sealed in PTFE tubes and placed into an Anton-Paar Microwave 3000 centrifuge with one tube containing an aqua regia blank. Samples were heated to 200 °C and held for 40 minutes before cooling to room temperature. Samples were diluted to 1% metal solutions (volume) using deionised water (18.2 MΩ cm). Support particulates were removed from solutions before analysis by filtering through a syringe filter-tip. Pd metal standards were prepared and measured first to calibrate the emission spectrometer. All standards, blanks and samples were vaporised and passed through a microwave induced plasma, exciting electrons in the sample. On their return to the ground state the element specific emission was detected using an Agilent Technologies 4100 MP-AES at four wavelengths of light corresponding to palladiums atomic transitions.

**Infrared CO Chemisorption Studies.** Fourier transform infrared (FTIR) transmission spectra were acquired using a Nicolet iS10 spectrometer at a spectral resolution of 2 cm<sup>-1</sup> and an accumulation of 64 scans. For each catalyst, ~25 mg of the catalyst was pressed to form a 13 mm diameter pellet. After placing the pellet inside of the transmission cell, the chamber was purged with He for

30 minutes (He flow rate = 30 mL/min), and a background spectrum was recorded. 10% CO/He was pulsed into the chamber for 30 seconds at a time at a flow rate of 10 mL/min. CO was dosed over the pellet until complete saturation of the pellet surface was achieved, normally 3–4 pulses. At this point the gas was switched to He for 30 minutes at 30 mL/min, removing gaseous and physisorbed CO from the chamber and pellet surface respectively.

**H<sub>2</sub> Temperature Programmed Reduction (H<sub>2</sub>-TPR).** Measurements were taken using an Anton Paar ChemBet Pulsar. Sample surfaces were purged at room temperature with Ar for 45 minutes. Analysis was performed in 4% H<sub>2</sub>/Ar (total flow rate = 25 mL/min) flow heating the sample from room temperature to 500 °C, where the ramp rate was 8 °C/min. The quantity of hydrogen consumed during the reduction process was determined by a thermal conductivity detector (TCD). Prior to TPR measurements, the TCD was calibrated at room temperature by pulsing pure H<sub>2</sub> (5 mL/min) in 125 mL of gas into the ChemBet chamber under pure Ar (total flow = 30 mL/min). Data acquisition and manipulation was performed using the TPR Win software.

**X-ray Absorption Fine Structure (XAFS).** XAFS studies were performed to examine the Pd oxidation state (X-ray Absorption Near-Edge structure/XANES) and the average Pd atom cluster size from the 1<sup>st</sup> shell coordination number (Extended X-ray Absorption Fine-Structure/EXAFS). Pd K-edge XAFS studies were carried out on the B18 beamline at the Diamond Light Source, Didcot, U.K. Measurements were performed in fluorescence mode using the QEXAFS setup with a fast-scanning Si(311) double-crystal monochromator, multi-element Ge and ion chamber detectors (for sample and reference foils respectively). Spectra was acquired at a time resolution of 1 min/spectrum (k<sub>max</sub> = 18), with 3 scans acquired per sample.

Cl K- and S K-edge XAFS measurements were performed to elucidate the presence, local geometry and oxidation state of the target element on the catalyst surface. Cl and S K-edge measurements were carried out on the BM28 beamline<sup>[98]</sup> (UK CRG - XMaS) at the European Synchrotron Facility, Grenoble, France. At the BM28 data was measured by running a variable point density macro (XESCAN.MAC – Extended Escan: Variable point density). In particular, energy scans can be performed for multiple consecutive energy regions, with equal or different step (variable point density). The samples were placed within a sample chamber and measurements performed under a vacuum of approximately 10<sup>-6</sup> mbar, to minimise air absorption at these ‘tender’ energies. The fluorescent signal was detected using a silicon drift diode detector and processed using a Mercury XIA digital signal processor. All spectra at Cl and S K-edges were acquired in fluorescence mode.<sup>[74]</sup>

#### XAFS data was processed using the Demeter software package<sup>[99,100]</sup>

**Catalytic Studies.** Furfural hydrogenation was performed at 50 °C using a stainless steel reactor (30 mL capacity), equipped with a heater, mechanical stirrer, gas supply system and thermometer. A fresh solution of furfural (10 mL, 0.3 M in 2-propanol) was placed into the reactor along with the desired quantity of catalyst (furfural/metal = 500 mol/mol). The reaction vessel was purged three times with 3 bar N<sub>2</sub> before being depressurised and again pressurised with H<sub>2</sub> to 5 bar and sealed. The mixture was left to reach 50 °C before being mechanically stirred (1000 rpm), to ensure kinetic regime conditions. At the end of the reaction, the autoclave was cooled to room temperature (25 °C), and pressure was relieved. The process of pressurising the vessel was repeated after reaction samples were withdrawn. Reaction samples were removed periodically (0.2 mL) and mixed with the internal solvent (2-propanol) and

external standard (dodecanol) before being analysed in an Agilent 6890 gas chromatograph equipped with a Zebron ZBS 60 m × 0.32 mm × 1 μm column. Authentic products (FA, THFA, etc.) were analysed to determine separation times. Quantitative analyses were performed using the external standard method, whereby GC peak area of each product was compared against a known standard (dodecanol). Unidentified ether products were identified using gas chromatograph-mass spectroscopy (GC-MS) (Figure S13). Aliquots of the reaction mixture were analysed using a Thermo Scientific ISQ QD, equipped with an Agilent VF-5 ms column, 60 m × 0.32 mm × 1 μm (inner diameter thickness).

#### Data Access Statement

The data that support the findings of this study are openly available via the University of Southampton DOI service at <http://doi.org/10.5258/SOTON/D2011>.

#### Acknowledgements

*The authors wish to acknowledge N. Ramanan and V. Celorrio for measuring Pd NP samples as part of the UK Catalysis Hub block access grant (BAG) (SP19850) on the B18 beamline at the Diamond Light Source, U.K. XMaS is a UK national research facility supported by EPSRC. We are grateful to all the beamline team staff for their support (experiment number CH5827). The RCaH core staff are also acknowledged for use of facilities. The electron microscopy department of Johnson Matthey Technology Centre, Sonning Common are acknowledged for their support in acquiring STEM HAADF and EDX images of fresh and used Pd/TiO<sub>2</sub> catalysts. D.D. acknowledges funded received through the UK Catalysis Hub and the UK Catalysis Hub is kindly thanked for resources and support provided via our membership of the UK Catalysis Hub Consortium and funded by EPSRC grant: EP/K014706/2, EP/K014668/1, EP/K014854/1, EP/K014714/1 or EP/M013219/1. P.P.W and K.M.H.M acknowledge the STFC GCRF START project for funding the position of K.M.H.M: ST/R002754/1.*

#### Conflict of Interest

The authors declare no conflict of interest.

**Keywords:** furfural hydrogenation · hydrogen spillover · palladium nanoparticles · sol-immobilization · X-ray absorption spectroscopy

- [1] B. R. Cuenya, *Thin Solid Films* **2010**, *518*, 3127–3150.
- [2] J. Polte, T. T. Ahner, F. Delissen, S. Sokolov, F. Emmerling, A. F. Thünemann, R. Kraehnert, *J. Am. Chem. Soc.* **2010**, *132*, 1296–1301.
- [3] E. K. Dann, E. K. Gibson, C. R. A. Catlow, P. Collier, T. E. Erden, D. Gianolio, C. Hardacre, A. Kroner, A. Raj, A. Goguet, P. P. Wells, *Chem. Mater.* **2017**, *29*, 7515–7523.
- [4] E. K. Dann, E. K. Gibson, R. H. Blackmore, C. R. A. Catlow, P. Collier, A. Chutia, T. E. Erden, C. Hardacre, A. Kroner, M. Nachtegaal, A. Raj, S. M. Rogers, S. F. R. Taylor, P. Thompson, G. F. Tierney, C. D. Zeinalipour-Yazdi, A. Goguet, P. P. Wells, *Nat. Catal.* **2019**, *2*, 157–163.

- [5] K. Nakaso, B. Han, K. H. Ahn, M. Choi, K. Okuyama, *J. Aerosol Sci.* **2003**, *34*, 869–881.
- [6] C. Lam, Y. F. Zhang, Y. H. Tang, C. S. Lee, I. Bello, S. T. Lee, *J. Cryst. Growth* **2000**, *220*, 466–470.
- [7] P. K. Khanna, P. V. More, J. P. Jawalkar, B. G. Bharate, *Mater. Lett.* **2009**, *63*, 1384–1386.
- [8] S. M. Rogers, C. R. A. Catlow, C. E. Chan-Thaw, D. Gianolio, E. K. Gibson, A. L. Gould, N. Jian, A. J. Logsdail, R. E. Palmer, L. Prati, N. Dimitratos, A. Villa, P. P. Wells, *ACS Catal.* **2015**, *5*, 4377–4384.
- [9] G. Mountrichas, S. Pispas, E. I. Kamitsos, *J. Phys. Chem. C* **2014**, *118*, 22754–22759.
- [10] G. F. Tierney, D. Decarolis, N. Abdullah, S. M. Rogers, S. Hayama, B. de Gutierrez, A. Villa, C. R. A. Catlow, P. Collier, N. Dimitratos, P. P. Wells, *Nanoscale Adv.* **2019**, *1*, 2546–2552.
- [11] N. Moloto, N. Revaprasadu, P. L. Musetha, M. J. Moloto, *J. Nanosci. Nanotechnol.* **2009**, *9*, 4760–4766.
- [12] N. Dimitratos, A. Villa, L. Prati, C. Hammond, C. E. Chan-Thaw, J. Cookson, P. T. Bishop, *Appl. Catal. A* **2016**, *514*, 267–275.
- [13] O. Rac, P. Suchorska-Woźniak, M. Fiedot, H. Teterycz, *Beilstein J. Nanotechnol.* **2014**, *5*, 2192–2201.
- [14] S. Campisi, M. Schiavoni, C. E. Chan-Thaw, A. Villa, *Catalysts* **2016**, *6*, 1–21.
- [15] S. H. Pang, C. A. Schoenbaum, D. K. Schwartz, J. W. Medlin, *Nat. Commun.* **2013**, *4*, 1–6.
- [16] A. Corma, S. Iborra, A. Veltz, *Chem. Rev.* **2007**, *107*, 2411–2502.
- [17] Y. Nakagawa, H. Nakazawa, H. Watanabe, K. Tomishige, *ChemCatChem* **2012**, *4*, 1791–1797.
- [18] S. M. Rogers, C. R. A. Catlow, C. E. Chan-Thaw, A. Chutia, N. Jian, R. E. Palmer, M. Perdjón, A. Thetford, N. Dimitratos, A. Villa, P. P. Wells, *ACS Catal.* **2017**, *7*, 2266–2274.
- [19] O. Aldosari, H. Alshammari, M. Alhumaimess, I. Wawata, *Turk. J. Chem.* **2019**, *43*, 24–38.
- [20] J. P. Lange, E. van der Heide, J. van Buijtenen, R. Price, *ChemSusChem* **2012**, *5*, 150–166.
- [21] S. Chen, R. Wojcieszak, F. Dumeignil, E. Marceau, S. Royer, *Chem. Rev.* **2018**, *118*, 11023–11117.
- [22] Y. Nakagawa, M. Tamura, K. Tomishige, *ACS Catal.* **2013**, *3*, 2655–2668.
- [23] Y. Wang, D. Zhao, D. Rodríguez-Padrón, C. Len, *Catalysts* **2019**, *9*, 1–33.
- [24] A. Gniewek, A. M. Trzeciak, J. J. Ziółkowski, L. Képiński, J. Wrzyszczyk, W. Tylus, *J. Catal.* **2005**, *229*, 332–343.
- [25] H. Hei, H. He, R. Wang, X. Liu, G. Zhang, *Soft Nanosci. Lett.* **2012**, *2*, 34–40.
- [26] K. H. Leong, H. Y. Chu, S. Ibrahim, P. Saravanan, *Beilstein J. Nanotechnol.* **2015**, *6*, 428–437.
- [27] L. Espinosa-Alonso, K. P. de Jong, B. M. Weckhuysen, *Phys. Chem. Chem. Phys.* **2010**, *12*, 97–107.
- [28] N. Dimitratos, J. A. Lopez-Sanchez, D. Morgan, A. F. Carley, R. Tiruvalam, C. J. Kiely, D. Bethell, G. J. Hutchings, *Phys. Chem. Chem. Phys.* **2009**, *11*, 5142–5153.
- [29] F. Porta, L. Prati, M. Rossi, S. Coluccia, G. Martra, *Catal. Today* **2000**, *61*, 165–172.
- [30] N. S. Figoli, P. C. L'Argentiere, *J. Mol. Catal. A* **1997**, *122*, 141–146.
- [31] P. Albers, J. Pietsch, S. F. Parker, *J. Mol. Catal. A* **2001**, *173*, 275–286.
- [32] L. J. Hoyos, M. Primet, H. Pralialud, I. U. Claude, B. Lyon, A. A. Einstein, *J. Chem. Soc. Faraday Trans.* **1992**, *88*, 3367–3373.
- [33] P. Frank, B. Hedman, R. M. K. Carlson, T. A. Tyson, A. L. Roe, K. O. Hodgson, *Biochemistry* **1987**, *26*, 4975–4979.
- [34] S. Pongpiachan, K. Thumanu, C. Kositanont, K. Schwarzer, J. Prietzel, P. Hirunyatrakul, I. Kittikoon, *J. Anal. Chem.* **2012**, *2012*, 1–12.
- [35] H. Lichtenberg, A. Prange, U. Steiner, E.-C. Oerke, J. Hormes, *J. Phys. Conf. Ser.* **2009**, *190*, 0–4.
- [36] F. Jalilvand, *Chem. Soc. Rev.* **2006**, *35*, 1256–1268.
- [37] G. Almkvist, K. Boye, I. Persson, *J. Synchrotron Radiat.* **2010**, *17*, 683–688.
- [38] S. C. Cook, J. D. Padmos, P. Zhang, *J. Chem. Phys.* **2008**, *128*, 154705.
- [39] C. A. Schneider, W. S. Rasband, K. W. Eliceiri, *Nat. Methods* **2012**, *9*, 671–675.
- [40] Y. Zhao, L. Jia, J. A. Medrano, J. R. H. Ross, L. Le, *ACS Catal.* **2013**, *3*, 2341–2352.
- [41] V. Vorotnikov, G. Mpourmpakis, D. G. Vlachos, *ACS Catal.* **2012**, *2*, 2496–2504.
- [42] K. Föttinger, W. Emhofer, D. Lennon, G. Rupprechter, *Top. Catal.* **2017**, *60*, 1722–1734.
- [43] M. Bowker, P. Stone, R. Bennett, N. Perkins, *Surf. Sci.* **2002**, *497*, 155–165.
- [44] C. D. Zeinalipour-Yazdi, D. J. Willock, L. Thomas, K. Wilson, A. F. Lee, *Surf. Sci.* **2016**, *646*, 210–220.
- [45] H. Zhu, Z. Qin, W. Shan, W. Shen, J. Wang, *J. Catal.* **2004**, *225*, 267–277.
- [46] K. I. Hadjiivanov, G. N. Vayssilov, *Adv. Catal.* **2002**, *47*, 307–511.
- [47] E. V. Benvenuti, L. Franken, C. C. Moro, *Langmuir* **1999**, *15*, 8140–8146.
- [48] A. Bourane, O. Dulaurent, D. Bianchi, *J. Catal.* **2000**, *196*, 115–125.
- [49] S. Bertarione, D. Scarano, A. Zecchina, V. Johánek, J. Hoffmann, S. Schauermann, M. M. Frank, J. Libuda, G. Rupprechter, H.-J. Freund, *J. Phys. Chem. B* **2004**, *108*, 3603–3613.
- [50] T. Lear, R. Marshall, J. A. Lopez-sanchez, S. D. Jackson, T. M. Klapötke, G. Rupprechter, H. Freund, D. Lennon, *J. Chem. Phys.* **2005**, *123*, 1–13.
- [51] A. Gaur, B. D. Shrivastava, H. L. Nigam, *Proc. Indian Natl. Sci. Acad. Part B* **2013**, *79*, 921–966.
- [52] P. P. Wells, E. M. Crabb, C. R. King, R. Wiltshire, B. Billsborrow, D. Thompsett, A. E. Russell, *Phys. Chem. Chem. Phys.* **2009**, *11*, 5773–5781.
- [53] S. Yilmaz, S. Ucar, L. Artok, H. Gulec, *Appl. Catal. A* **2005**, *287*, 261–266.
- [54] H. Rojas, J. J. Martínez, P. Reyes, *Dyna* **2010**, *163*, 151–159.
- [55] S. Aljani, S. Capelli, S. Cattaneo, M. Schiavoni, C. Evangelisti, K. M. H. Mohammed, P. P. Wells, F. Tessore, A. Villa, *Catalysts* **2020**, *10*, 1–16.
- [56] L. Prati, A. Villa, *Acc. Chem. Res.* **2014**, *47*, 855–863.
- [57] Z. Liu, O. L. Lanier, A. Chauhan, *Nanomaterials* **2020**, *10*, 1–16.
- [58] S. R. Chowdhury, P. S. Roy, S. K. Bhattacharya, *Adv. Nat. Sci. Nanosci. Nanotechnol.* **2017**, *8*, 1–10.
- [59] S. Scurti, E. Monti, E. Rodríguez-Aguado, D. Caretti, J. A. Cecilia, N. Dimitratos, *Nanomaterials* **2021**, *11*, DOI 10.3390/nano11040879.
- [60] S. Haesuwannakij, T. Kimura, Y. Furutani, K. Okumura, K. Kokubo, T. Sakata, H. Yasuda, Y. Yakiyama, H. Sakurai, *Sci. Rep.* **2017**, *7*, 1–8.
- [61] P. Lanzafame, G. Papanikolaou, S. Perathoner, G. Centi, M. Migliori, E. Catizzone, A. Aloise, G. Giordano, *Catal. Sci. Technol.* **2018**, *8*, 1304–1313.
- [62] M. E. Manriquez, T. López, R. Gómez, J. Navarrete, *J. Mol. Catal. A* **2004**, *220*, 229–237.
- [63] S. Campisi, C. E. Chan-Thaw, L. E. Chinchilla, A. Chutia, G. A. Botton, K. M. H. Mohammed, N. Dimitratos, P. P. Wells, A. Villa, *ACS Catal.* **2020**, *10*, 5483–5492.
- [64] R. Prins, *Chem. Rev.* **2012**, *112*, 2714–2738.
- [65] T. Huizinga, R. Prins, *J. Phys. Chem.* **1981**, *85*, 2156–2158.
- [66] Y.-K. Peng, H.-L. Chou, S. C. E. Tsang, *Chem. Sci.* **2018**, *9*, 2493–2500.
- [67] C. Lv, X. Lan, F. Li, L. Wang, L. Xiao, C. Wang, J. Shi, S. Yu, *Catal. Sci. Technol.* **2020**, *10*, 690–699.
- [68] V. V. Gorodetskii, A. V. Matveev, *Hydrogen Spillover in H<sub>2</sub> Oxidation on Pd-Ti<sub>3</sub>+TiO<sub>2</sub>*, Elsevier Science B. V., **2001**.
- [69] D. Padovan, A. Al-Nayili, C. Hammond, *Green Chem.* **2017**, *19*, 2846–2854.
- [70] D. Wu, W. Y. Hernández, S. Zhang, E. I. Vovk, X. Zhou, Y. Yang, A. Y. Khodakov, V. V. Ordonsky, *ACS Catal.* **2019**, *9*, 2940–2948.
- [71] R. B. Boysen, R. K. Szilagy, *Inorg. Chim. Acta* **2008**, *361*, 1047–1058.
- [72] R. L. Barton, D. J. Gardenghi, W. C. Stolte, R. K. Szilagy, *J. Phys. Chem. A* **2015**, *119*, 5579–5586.
- [73] G. Malta, S. A. Kondrat, S. J. Freakley, D. J. Morgan, E. K. Gibson, P. P. Wells, M. Aramini, D. Gianolio, P. B. J. Thompson, P. Johnston, G. J. Hutchings, *Chem. Sci.* **2020**, *11*, 7040–7052.
- [74] P. B. J. J. Thompson, B. N. Nguyen, R. Nicholls, R. A. Bourne, J. B. Brazier, K. R. J. J. Lovelock, S. D. Brown, D. Wermeille, O. Bikondoa, C. A. Lucas, T. P. A. A. Hase, M. A. Newton, *J. Synchrotron Radiat.* **2015**, *22*, 1426–1439.
- [75] M. A. Newton, R. Nicholls, J. B. Brazier, B. N. Nguyen, C. J. Mulligan, K. Hellgardt, E. M. Barreiro, H. Emerich, K. K. Mii, I. Snigireva, P. B. J. Thompson, K. Kuok, M. Hii, I. Snigireva, P. B. J. Thompson, *Catal. Struct. React.* **2017**, *3*, 149–156.
- [76] C. Amorim, M. A. Keane, *J. Colloid Interface Sci.* **2008**, *322*, 196–208.
- [77] N. Lingaiah, P. S. Sai Prasad, P. Kanta Rao, F. J. Berry, L. E. Smart, *Catal. Commun.* **2002**, *3*, 391–397.
- [78] G. Neri, M. G. Musolino, C. Milone, D. Pietropaolo, S. Galvagno, *Appl. Catal. A* **2001**, *208*, 307–316.
- [79] M. Bonarowska, B. Burda, W. Juszczak, J. Pielaszek, Z. Kowalczyk, Z. Karpiński, *Appl. Catal. B* **2001**, *35*, 13–20.
- [80] L. M. Gómez-Sainero, X. L. Seoane, J. L. G. Fierro, A. Arcoya, *J. Catal.* **2002**, *209*, 279–288.
- [81] U. S. Ozkan, M. W. Kumthekar, G. Karakas, *Catal. Today* **1998**, *40*, 3–14.
- [82] T. Hengsawad, T. Jindarat, D. E. Resasco, S. Jongpatiwut, *Appl. Catal. A* **2018**, *566*, 74–86.
- [83] E. Nowicka, S. Althahban, T. D. Leah, G. Shaw, D. Morgan, C. J. Kiely, A. Roldan, G. J. Hutchings, *Sci. Technol. Adv. Mater.* **2019**, *20*, 367–378.

- [84] G. V. A. Martins, G. Berlier, C. Bisio, S. Coluccia, H. O. Pastore, L. Marchese, *J. Phys. Chem. C* **2008**, *112*, 7193–7200.
- [85] S. B. Ziemecki, G. A. Jones, *J. Catal.* **1985**, *95*, 621–622.
- [86] S. B. Ziemecki, G. A. Jones, D. G. Swartzfager, R. L. Harlow, J. Faber, *J. Am. Chem. Soc.* **1985**, *107*, 4547–4548.
- [87] S. Nakamura, T. Yasui, *J. Catal.* **1970**, *17*, 366–374.
- [88] O. Balmes, A. Resta, D. Wermeille, R. Felici, M. E. Messing, K. Deppert, Z. Liu, M. E. Grass, H. Bluhm, R. Van Rijn, J. W. M. Frenken, R. Westerström, S. Blomberg, J. Gustafson, J. N. Andersen, E. Lundgren, *Phys. Chem. Chem. Phys.* **2012**, *14*, 4796–4801.
- [89] M. Bowker, L. Cookson, J. Bhantoo, A. Carley, E. Hayden, L. Gilbert, C. Morgan, J. Counsell, P. Yaseneva, *Appl. Catal. A* **2011**, *391*, 394–399.
- [90] M. Crespo-Quesada, S. Yoon, M. Jin, A. Prestianni, R. Cortese, F. Cárdenas-Lizana, D. Duca, A. Weidenkaff, L. Kiwi-Minsker, *J. Phys. Chem. C* **2015**, *119*, 1101–1107.
- [91] M. W. Tew, M. Nachtegaal, M. Janousch, J. A. Van Bokhoven, T. Huthwelker, J. A. van Bokhoven, *Phys. Chem. Chem. Phys.* **2012**, *14*, 5761–5768.
- [92] J. A. McCaulley, *Phys. Rev. B* **1993**, *47*, 4873–4879.
- [93] W. Jones, P. P. Wells, E. K. Gibson, A. Chutia, I. P. Silverwood, C. R. A. Catlow, M. Bowker, *ChemCatChem* **2019**, *11*, 4334–4339.
- [94] A. L. Bugaev, O. A. Usoltsev, A. A. Guda, K. A. Lomachenko, I. A. Pankin, Y. V. Rusalev, H. Emerich, E. Groppo, R. Pellegrini, A. V. Soldatov, J. A. van Bokhoven, C. Lamberti, *J. Phys. Chem. C* **2018**, *122*, 12029–12037.
- [95] A. L. Bugaev, A. A. Guda, I. A. Pankin, E. Groppo, R. Pellegrini, A. Longo, A. V. Soldatov, C. Lamberti, *Catal. Today* **2019**, *336*, 40–44.
- [96] A. L. Bugaev, A. A. Guda, K. A. Lomachenko, L. A. Bugaev, A. V. Soldatov, *Bull. Russ. Acad. Sci. Phys.* **2015**, *79*, 1180–1185.
- [97] Y.-F. Han, D. Kumar, C. Sivadinarayana, A. Clearfield, D. W. Goodman, *Catal. Lett.* **2004**, *94*, 131–134.
- [98] P. Thompson, O. Bikondoa, L. Bouchenoire, S. Brown, M. Cooper, T. Hase, C. Lucas, D. Wermeille, *AIChE Conf. Proc.* **2019**, *2054*, 060030.
- [99] B. Ravel, *X-Ray Absorpt. X-Ray Emiss. Spectrosc. Theory Appl.* (Eds.: J. A. van Bokhoven, C. Lamerbiti), Wiley, **2016**, p. 283.
- [100] B. Ravel, M. Newville, *J. Synchrotron Radiat.* **2005**, *12*, 537–541.

---

Manuscript received: July 9, 2021

Revised manuscript received: October 4, 2021

Accepted manuscript online: October 10, 2021

Version of record online: November 2, 2021